Scattering zones in quantum speckle propagation

Shaurya Aarav,[*] S. A. Wadood, and Jason W. Fleischer[†]
Department of Electrical and Computer Engineering, Princeton University, Princeton, New Jersey 08544, USA

(Received 11 July 2025; revised 11 June 2026; accepted 14 September 2026; published 30 October 2026)

Quantum speckles exhibit significantly richer behavior than their classical counterparts due to their higher dimensionality. A simple example is the far-field speckle pattern in one-dimensional (1D) light scattering: Classical light forms 1D speckles defined by the numerical aperture, whereas biphoton scattering depends in addition on the photon correlation length, forming two-dimensional elliptical speckles. To date, the behavior of quantum speckles for shorter propagation distances has not been considered. We remedy this here by considering the paraxial evolution of two-photon entanglement at arbitrary propagation distances from a scatterer. We show, theoretically, numerically, and experimentally, that the two length scales of the biphoton introduce a new Fresnel regime between the conventional near and far fields. Further, we show that the quantum near field is characterized by speckles with a square shape that remain constant during propagation. In contrast, the intermediate regime can be engineered to have a constant speckle size along the sum coordinate but a linearly expanding speckle size along the difference coordinate, with a speckle shape that transitions from square to elliptical. The results merge quantum coherence with scattering statistics and suggest new regimes of operation for correlation-based quantum sensing and imaging.

DOI: 10.1103/ymwh-j65z

I. INTRODUCTION

Speckle is the result of random interference, such as that caused by scattering media, and depends sensitively on both phase and statistics. While its use in vibrometry has been recognized for decades [1], its presence in other fields has been considered detrimental. Even though the speckle intensity is random, with an increased understanding of the underlying correlations and an exponential increase in computing power, speckle has become appreciated as a resource for imaging tasks and information processing. Examples include enhanced focusing [2], lensless imaging [3–5], three-dimensional imaging [6,7], and reservoir computing [8].

Speckles can be correlated in different degrees of freedom, and their usefulness often depends on the particular problem. For example, local shift invariance is useful for memory-effect-based imaging of two-dimensional (2D) objects [9], intensity statistics has utility in optical manipulation [10,11], and wavelength correlations allow for spectrum analysis [12]. Here, we focus on the spatial correlations of speckles in the transverse direction to highlight the differences between classical and quantum (biphoton) speckle propagation. We consider the simplest case: light of a single wavelength λ, propagation with one transverse dimension, and transmission through a thin scattering medium with correlation length σ_0 (the reflection case is similar).

In analogy with free-space propagation, the propagation of classical speckles away from a scattering medium is conventionally defined by a near field and a far field. In the latter, light scattered from different regions of the medium can overlap, resulting in a speckle size that grows linearly with distance from the scatterer (as explained by the van Cittert-Zernike theorem [13]). In the former (sometimes called the deep Fresnel regime), different regions propagate individually, and the speckle size stays constant. The crossover distance is determined by the correlation length σ_0 and the numerical aperture [14–17].

To date, studies of biphoton speckle propagation have been restricted to the far field, where the main observed difference from the classical case is the shape of the speckle [18,19]. This is because entangled photon pairs have an extra degree of freedom, the relative separation σ_- of their components, other than the overall beam size σ_+. The ratio of the two sizes causes the speckles to appear elliptical while still maintaining the linear scaling with propagation, like in the classical case.

Here, we show that the biphoton speckle (observed in photon correlations rather than intensity) exhibits even richer behavior when the propagation distance is shorter. Most significantly, quantum correlation introduces a new regime of speckle propagation, intermediate between the near and far fields. In this region, the sum coordinate correlation of the photon pairs can propagate without change, while the difference coordinate grows linearly. Moreover, the shape of the speckle is not, in general, elliptical. When both coordinates propagate unchanged, i.e., in the near field, the speckle shape is square. It is only in the far field that speckles are truly

[*]Present address: Sorbonne Université, CNRS, Institut des NanoSciences de Paris, INSP, F-75005 Paris, France.
[†]Contact author: jasonf@princeton.edu

Published by the American Physical Society under the terms of the Creative Commons Attribution 4.0 International license. Further distribution of this work must maintain attribution to the author(s) and the published article's title, journal citation, and DOI.

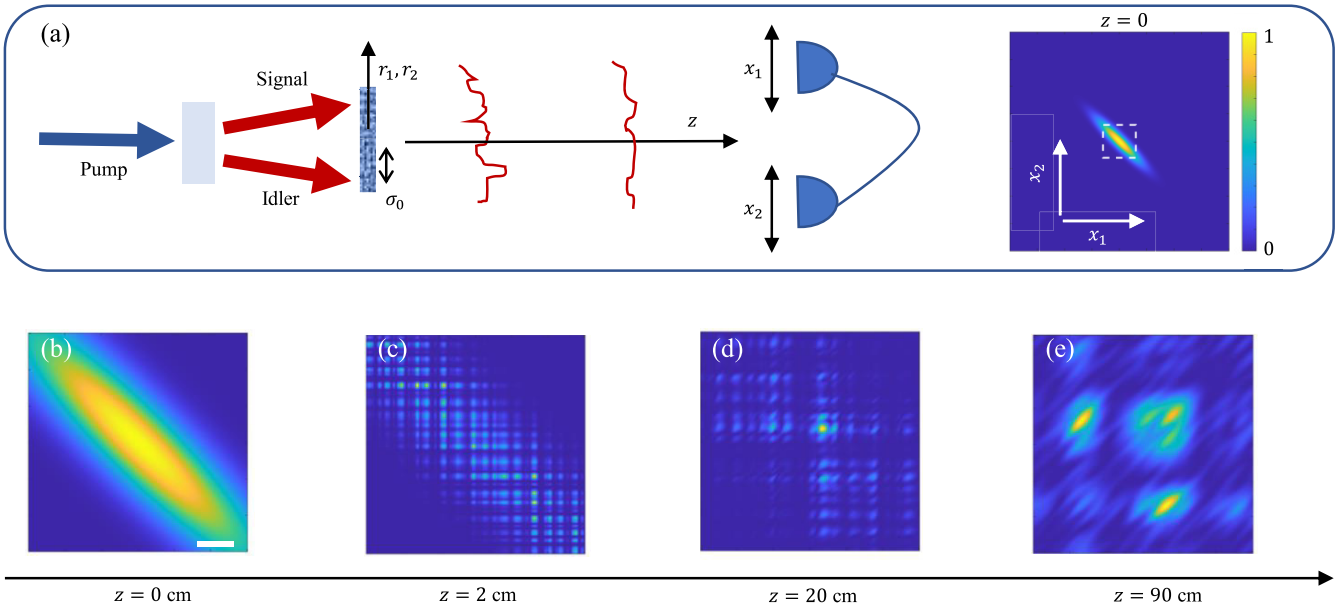


FIG. 1. Simulation of biphoton speckles with propagation. (a) Simulation scheme. Biphotons scatter from a medium with a correlation length σ_0, propagate a distance z, and are measured in coincidence. Right: Biphoton intensity at the scatterer plane $z = 0$. The dashed square indicates the cropped region of interest for the bottom row. (b)–(e) Evolution of the biphoton intensity with z. (b) Initial intensity. (c) At small propagation distances, the speckles are squarish in shape and appear in a gridlike lattice oriented along the antidiagonal. (d), (e) As z increases, the large-scale grid structure becomes more discrete and the speckle shape becomes more elliptical, with individual orientations along the diagonal. The scale bar for panels (b)–(e) is 0.5 mm.

elliptical. We support our theoretical results using simulations and experiments and discuss the implications of these results for higher photon number states.

II. THEORY

A schematic of our setup is shown in Fig. 1(a). Biphotons are generated by spontaneous parametric down-conversion (SPDC) [20], propagate through a thin scattering medium, and are measured in coincidence. Let $\psi_{\text{in}}(r_1, r_2)$ be the biphoton field just before the scatterer, where (r_1, r_2) are the positions of photons 1 (signal) and 2 (idler) on the scatterer plane. Under the Gaussian approximation, ψ_{in} can be written as [21,22]

$$\psi_{\text{in}} = e^{-\frac{(r_1-r_2)^2}{\sigma_-^2}} e^{-\frac{(r_1+r_2)^2}{\sigma_+^2}}, \tag{1}$$

where σ_+, σ_- depend on the pump profile and crystal thickness, repectively [20]. The specific Gaussian form is not essential for our subsequent analysis; we show it above to emphasize the existence of two different length scales in the input state. Without loss of generality, we operate in the near field of the crystal for the theoretical analysis. Physically, σ_+ determines the overall spatial extent of the beam when measuring single photons, while σ_- determines the extent of the signal photon when conditioned on the coincidence measurement of the idler photon. In the far field of the crystal, our results remain the same except for the swapping of the two parameters $\sigma_- \leftrightarrow \sigma_+$. Without loss of generality, we assumed the transverse spatial dimension to be one dimensional (1D), such that the joint probability density of the biphotons is 2D (x_1, x_2).

Due to the thin scatterer, each photon acquires a phase $\phi(r)$ such that the biphoton field after the scatterer $\psi_0 = \psi_{\text{in}}(r_1, r_2)e^{i\phi(r_1)}e^{i\phi(r_2)}$. For a classical field $E(r)$, where r is the transverse coordinate, the electric field just after the scatterer $E_0(r)$ and the electric field just before the scatterer $E_{\text{in}}(r)$ are related as $E_0(r) = E_{\text{in}}(r)e^{i\phi(r)}$. The presence of two phase terms for the biphoton case arises due to its two-photon nonclassical nature. Upon propagating a distance z, $\psi_0 \to \psi_z$, which we model using the Fresnel (paraxial) approximation (see Appendix A). We study the spatial structure of speckles using the biphoton correlation function $\Gamma_z = \langle \psi_z(r_1, r_2)\psi_z^*(r_1', r_2')\rangle$, where $\langle\cdot\rangle$ represents an ensemble average over many scatterer realizations and * denotes complex conjugate. See Appendix A for more details.

To make the calculation of Γ_z tractable, we follow Ref. [18] and make two assumptions. First, we assume that the scattered biphoton field exhibits Gaussian statistics, so that the correlation of the field and intensity are directly related. Second, we assume that the scatterer is strong, such that the correlation function at $z \to 0$ is

$$\Gamma_0 \approx R_0(\bar{r}_+, \bar{r}_-)\mu(\delta r_1, \delta r_2), \tag{2}$$

where $R_0(\bar{r}_+, \bar{r}_-)$ is the average biphoton intensity determining the coincidence for ψ_{in} and $\mu(\delta r_1, \delta r_2)$ is the correlation function of the scatterer. The width of μ is the scatterer correlation length σ_0, assumed the same along both coordinates. Details of the coordinate transforms are listed in Table I.

Apart from the wavelength λ, there are three other length parameters: σ_-, σ_+, and σ_0. Their combinations divide the axial direction into distinct regions, observed in the z evolution of the correlation function Γ_z. We assume a separation of length scales, such that the scatterer correlation length

TABLE I. Coordinate transforms.

$r_1 = \bar{r}_1 + \delta r_1$	and	$r_1' = \bar{r}_1 - \delta r_1$
$r_2 = \bar{r}_2 + \delta r_2$	and	$r_2' = \bar{r}_2 - \delta r_2$
$\bar{r}_+ = \bar{r}_1 + \bar{r}_2$	and	$\bar{r}_- = \bar{r}_1 - \bar{r}_2$
$\delta r_+ = \delta r_1 + \delta r_2$	and	$\delta r_- = \delta r_1 - \delta r_2$

$\sigma_0 \ll \sigma_-, \sigma_+$. The axial regions of propagation then become the following:

(1) *Far field*: $z > \sigma_0\sigma_+/\lambda$.

$$\Gamma_z = C\mathfrak{F}[R_0(\bar{r}_+, \bar{r}_-)]\left(\frac{1}{z\lambda}(\delta x_+, \delta x_-)\right) \times \mathfrak{F}[\mu(\delta r_1, \delta r_2)]\left(\frac{1}{z\lambda}(\bar{x}_+, \bar{x}_-)\right), \quad (3)$$

where C is a phase factor and $\mathfrak{F}$ denotes a Fourier transform. This result recovers the far-field speckle correlations obtained in Ref. [18], with elliptical speckles with widths $w_+ = z\lambda/\sigma_+$ and $w_- = z\lambda/\sigma_-$ along their respective axes. The field of view is determined by the scatterer properties, giving the $\pm$ widths $l_+ = l_- = z\lambda/\sigma_0$.

Note that the defining distance of the far-field regime is similar to that of single-photon speckles, with the beam width σ_+ replaced by the aperture size [15–17]. This width also determines the global properties of the beam, e.g., its field of view. The local properties, e.g., the speckle shape, are drastically different due to the biphotons being twice the dimension of single-photon speckles; elliptical speckles cannot exist in 1D.

(2) *Near field*: $z < \sigma_0\sigma_-/\lambda$.

$$\Gamma_z = R_0(\bar{x}_+, \bar{x}_-)\mu(\delta x_+, \delta x_-). \quad (4)$$

This result is similar to the near-field relation derived for single photons in [15–17]. In this region, the biphoton speckle size depends only on the scatterer correlation function. Since μ has the same width along both photon coordinates $\delta r_1, \delta r_2$, the speckles appear as *squares* of width $w_+ = w_- = \sigma_0$. The field of view is determined by the input state and is elliptical, with the $\pm$ widths given by $l_+ = \sigma_+$ and $l_- = \sigma_-$, respectively.

(3) *Intermediate field*: $\sigma_0\sigma_-/\lambda < z < \sigma_0\sigma_+/\lambda$.

This regime does not exist for single-photon speckles, as they lack the internal degrees of freedom necessary for scale separation during propagation.

III. SIMULATIONS

Here, we simulate the system shown in Fig. 1(a). The far-field of the SPDC beam is incident on the scattering medium; thus, the role of σ_- and σ_+ are swapped in Eq. (1). In what follows, we keep a constant wavelength $\lambda = 810$ nm and scatterer correlation length $\sigma_0 = 44\,\mu$m but vary the biphoton parameters σ_- and σ_+. In all cases, we observe the evolution of coincidence functions from the initial elliptical Gaussian intensity $|\psi_0|^2$ at $z = 0$ to the far field nearly a meter later. Details of the simulation are given in Appendix B.

Figures 1(b)–1(e) show propagation results for $\sigma_- = 1$ mm and $\sigma_+ = 5$ mm. As predicted, the near field $z^{\mathrm{NF}} < \sigma_0\sigma_-/\lambda = 5$ cm is characterized by a gridlike pattern of squarelike speckles [Fig. 1(c)] that smoothly elongate in the far field $z^{\mathrm{FF}} > \sigma_0\sigma_+/\lambda = 27$ cm. In the intermediate regime, the grid structure becomes more distinct and the orientation of the internal structures transitions to antidiagonal correlations.

To make our observations on speckle shape more concrete, we plot the speckle sizes for a given scatterer realization and different input state parameters (Fig. 2). For Fig. 2(a), the widths of the input states are $\sigma_+ = 1.8$ mm and $\sigma_- = 1$ mm, giving crossover distances for the near-field and far-field zones of $z^{\mathrm{NF}} \sim 5$ cm and $z^{\mathrm{FF}} \sim 9$ cm, respectively. Thus, we expect (and observe) the speckle size to be elliptical above these z values, with major axis length $w_+ \propto 1/\sigma_-$ and minor axis length $w_- \propto 1/\sigma_+$.

In Fig. 2(b), we increase the width of the input state to $\sigma_+ = 5$ mm while keeping the sum coordinate width $\sigma_- = 1$ mm the same. The near-field zone $z^{\mathrm{NF}} \lesssim 5$ cm thus remains the same, while the far-field zone increases to $z^{\mathrm{FF}} \gtrsim 27$ cm. This corresponds to the middle region between the near field and the far field, with the speckle size along one dimension increasing linearly with z and the speckle size along the perpendicular direction remaining flat. However, we do not see the expected transition to the far-field zone at $z = 27$ cm. This is because we calculated the critical value z^{FF} from a length-scale argument; in practice, the transition z^{FF} will

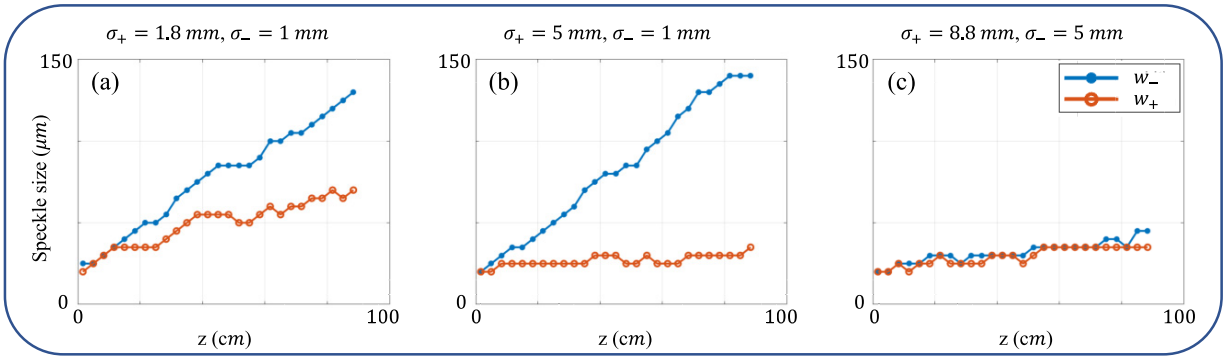


FIG. 2. Simulations of biphoton speckle size as a function of propagation distance z. The wavelength and scattering correlation length are fixed at $\lambda = 810$ nm and $\sigma_0 = 44\,\mu$m, while the biphoton input parameters $\{\sigma_-, \sigma_+\}$ are chosen such that the speckles are (a) in the far-field zone for the full range of z, (b) in the intermediate zone, and (c) in the near-field zone.

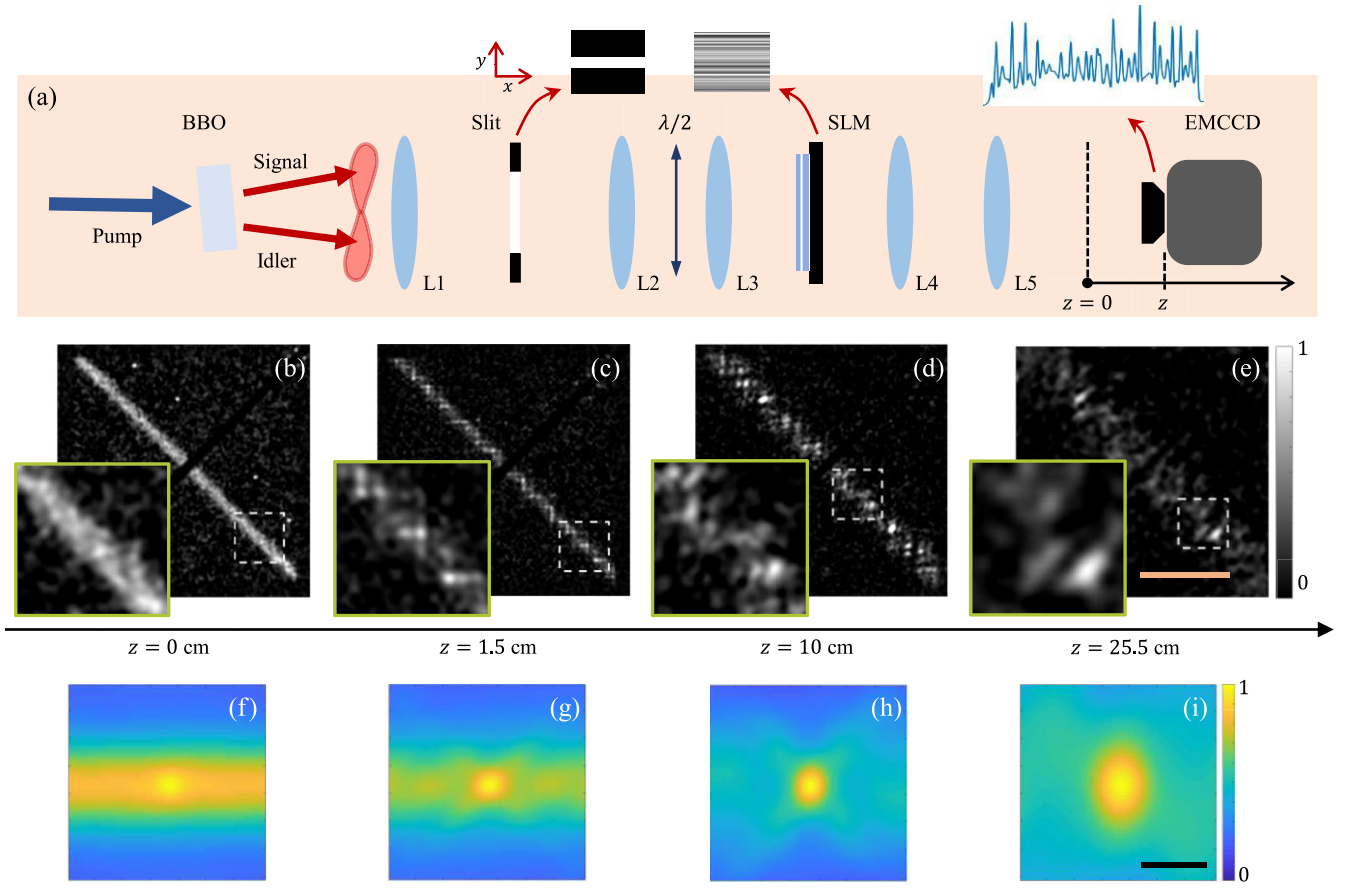


FIG. 3. Experimental results. (a) Experimental setup. In the first half, biphotons created in a BBO crystal via Type-1 SPDC are shaped into a quasi-1D beam. In the second half, the beam is polarized by a half-wave plate, acquires a random "scattering" phase from an SLM, and is imaged onto an EMCCD camera. Lens $L1$ performs an optical Fourier transform onto the slit, while lenses $\{L2, L3\}$ and $\{L4, L5\}$ are imaging relays. (b)–(e) Coincidence measurements at four propagation distances, depicting the evolution of biphoton speckles. Insets: Magnified images of region within the dashed white box. Each speckle image is normalized by the maximum value in its inset. Scale bar: 2.7 mm. (f)–(i) Speckle shape obtained by autocorrelation (cropped and rotated by 45° for better visualization). Speckles start with a rectangular structure in panel (g), but transition to an elliptical feature in the far field in panel (i). Panel (h) shows intermediate regimes where the speckle is neither rectangular nor completely elliptical. Scale bar: 0.37 mm.

depend on the exact functional forms of the scatterer correlation and the input state, i.e., the exact results from the full Fresnel integral [23].

In Fig. 2(c), we demonstrate the speckle behavior in the near-field zone. To represent this region, we use larger values of both biphoton widths of the input state: $\sigma_+ = 8.8$ mm and $\sigma_- = 5$ mm, giving critical distances $z^{\mathrm{NF}} \sim 27$ cm and $z^{\mathrm{FF}} \sim 47$ cm. Since σ_- now has the same width that σ_+ had in Fig. 2(b), we expect the same flat behavior with z. Indeed, Fig. 2(c) shows that the widths in both directions remain flat. This behavior corresponds to the square speckles in Fig. 1(c) and is characteristic of quantum light propagation in the near-field region. The evolution of the singles intensity with z is described in Appendix D.

IV. EXPERIMENTS

Our experimental setup is shown in Fig. 3(a). A 5 mm × 5 mm × 3 mm BBO (beta barium borate) crystal is illuminated by a 405 nm laser pump. The crystal is rotated slightly to operate in the collinear regime and placed at the back focal plane of lens $L1$ with focal length 10 cm. This lens projects the far-field of the crystal on to a slit, which reshapes it to a 1D profile, before acquiring a random phase imprinted by a spatial light modulator (SLM). We perform coincidence imaging of the biphotons using an Andor iXon Ultra EMCCD camera and use the scheme outlined in Refs. [24–27] by taking 1–2 million frames at different exposure times. Different propagation distances are recorded by moving the camera axially.

Coincidence images and their autocorrelations are shown in Figs. 3(b)–3(i). At $z = 0$ [Fig. 3(b)], we see the anticorrelation diagonal typical of the far field of an SPDC setup. The effect of the phase scattering is not yet visible, as this is the image plane of the SLM. Moving the EMCCD to $z = 1.5$ cm [Fig. 3(c)], we observe square-shaped speckles appearing in a rectangular gridlike pattern, indicative of the quantum near-field region. The speckle shape can be better seen in the autocorrelation image (g). Moving the detector to $z =$ 10 cm [Fig. 3(d)], we see the speckles become more elliptical, confirmed in the autocorrelation image (h). Finally, we moved the detector to $z = 25.5$ cm [Fig. 3(e)]. The speckles now are markedly elliptical [again better visualized in the

autocorrelation (i)], demonstrating the transition to the far-field region.

V. DISCUSSION

Because of the added degree of freedom, biphoton dynamics do not follow simply from quantization of classical near-field results. Coupled with propagation, the high-dimensional nature of biphotons enables entirely new speckle applications. In the near field, the use of biphotons instead of classical light can improve the capabilities of existing speckle measurement techniques, e.g., lensless imaging [5], depth sensing [6], and material characterization [14]. In the intermediate zone, the advantages of quantum imaging (such as higher resolution [26], increased sensitivity [23], and improved noise properties [28]) suggest the intriguing possibility to probe independently, and simultaneously, the near- and far-field speckle behavior of a scatterer. The near-field and intermediate zones also offer possibly novel connections between speckle statistics and entanglement [29,30] and associated improvements to adaptive quantum optics [31,32]. We note that the biphoton speckle propagation differs from the classical case in three distinct ways: First, it accrues the scattering phase twice; second, its propagation involves the free-space transfer function twice too; and third, the measurements are the correlation of photons instead of intensities in the classical case.

There are significant implications of our work for higher-order photon correlations, which are essential for metrology [33], imaging [34,35], and computing [36]. While classical single-photon speckles cannot uniquely quantify biphoton speckle statistics, the latter do contain information about higher-order speckles. For example, the biphoton wavefunction uniquely determines all higher-order coincidence probabilities (and hence the speckle statistics) of multimode squeezed states generated via down-conversion [37,38]. Because multiphoton correlations can offer N-fold enhancements in phase sensitivity [39] and both transverse and axial resolution [34,35], multiphoton speckles can offer more degrees of freedom and structure upon propagation.

VI. CONCLUSIONS

In this work, we studied the propagation behavior of biphoton speckles due to a thin-phase scatterer. Unlike their classical counterparts, biphoton speckles exhibit a distinct intermediate propagation region between the near and far fields. The crossover distances depend on the correlation length of the scatterer, the correlation lengths of the biphoton along its sum-difference coordinates, and the wavelength. Different ratios of these lengths correspond to differences in speckle shape, statistics, and dynamics. For higher-order photon number states, there are more internal degrees of freedom, with similar but more varied opportunities for separation of scales. Our work therefore informs the generation, propagation, and control over the scattering of high-dimensional entangled states.

ACKNOWLEDGMENTS

We thank Dr. Abhinandan Bhattacharjee for the discussions regarding the measurement technique. This work was supported by AFOSR Grants No. FA9550-19-1-0167 and No. FA9550-18-1-0219. We also thank AFOSR Grant No. FA9550-23-1-0221 for partial support.

DATA AVAILABILITY

The data that support the findings of this article are not publicly available upon publication because it is not technically feasible and/or the cost of preparing, depositing, and hosting the data would be prohibitive within the terms of this research project. The data are available from the authors upon reasonable request.

APPENDIX A: THEORY

The evolution of biphotons with propagation can be written as

$$\psi_z = \iint \psi_0(r_1, r_2) h_z(r_1, x_1) h_z(r_2, x_2) dr_1 dr_2, \tag{A1}$$

where the free-space transfer function (under the Fresnel approximation) $h_z(r_j, x_j) = e^{-ik_0(r_j - x_j)^2/2z}$, $k_0 = 2\pi/\lambda$, and $r_{1,2}, x_{1,2}$ denote the input- and output-plane coordinates, respectively. The biphoton wavefunction after the scatterer is $\psi_0 = \psi_{\text{in}}(r_1, r_2) e^{i\phi(r_1)} e^{i\phi(r_2)}$, with $\phi(r)$ being the phase imparted by the scatterer. We note that the free-space propagation of a classical electric field follows the equation $E(x, z) = \int E_0(r) h_z(r, x) dr$, where $E_0(r)$ is the field at $z = 0$. This contrasts with the biphoton wavefunction propagation that accrues the transfer function twice. The corresponding biphoton correlation function $\Gamma_z = \langle \psi_z(x_1, x_2) \psi_z^*(x_1', x_2') \rangle$ is thus

$$\Gamma_z = C \int \Gamma_0 e^{-i\frac{k_0}{2z}[(r_1 - x_1)^2 - (r_2 - x_2)^2]} \times e^{i\frac{k_0}{2z}[(r_1' - x_1')^2 + (r_2' - x_2')^2]} dr_1 dr_2 dr_1' dr_2', \tag{A2}$$

where $C = e^{-i\frac{k_0}{z}(\delta x_+ \bar{x}_+ + \delta x_- \bar{x}_-)}$ is a phase term (expressed in terms of the $\pm$ coordinates listed in Table I). Using the decomposition $\Gamma_0 \approx R_0(\bar{r}_+, \bar{r}_-) \mu(\delta r_1, \delta r_2)$ [Eq. (2)] and integrating along $\delta r_+, \delta r_-$ gives

$$\Gamma_z = C \int R_0(\bar{r}_+, \bar{r}_-) e^{-i\frac{k_0}{z}[-\delta x_+ \bar{r}_+ - \delta x_- \bar{r}_-]} \times \mathfrak{F}[\mu(\delta r_1, \delta r_2)] \left(\frac{1}{z\lambda} (\bar{x}_+ - \bar{r}_+, \bar{x}_- - \bar{r}_-) \right) d\bar{r}_+ d\bar{r}_-. \tag{A3}$$

Below, we use this expression to calculate Fresnel propagation in the near and far fields.

1. Far field

We define the far field such that the propagation distance $z > \sigma_0 \sigma_+ / \lambda$. This assumption greatly simplifies Eq. (A3). It leads to $\mathfrak{F}[\mu(\delta r_1, \delta r_2)](\frac{1}{z\lambda}(\bar{x}_+ - \bar{r}_+, \bar{x}_- - \bar{r}_-)) \approx \mathfrak{F}[\mu(\delta r_1, \delta r_2)](\frac{1}{z\lambda}(\bar{x}_+, \bar{x}_-))$. This is applicable because the width of $\mathfrak{F}[\mu(\delta r_1, \delta r_2)]$ along the two dimensions is $z\lambda/\sigma_0$, whereas the width of $R_0(\bar{r}_+, \bar{r}_-)$ is (σ_+, σ_-) along the two

dimensions. Since we assumed $\sigma_- < \sigma_+$, the far-field condition implies that $\mathfrak{F}[\mu]$ is much broader than R_0 as a function of $(\bar{r}_+, \bar{r}_-)$, hence justifying to omit $\mathfrak{F}[\mu]$'s dependence on $(\bar{r}_+, \bar{r}_-)$. We can then integrate Eq. (A3) to get

$$\Gamma_z = C\mathfrak{F}[R_0(\bar{r}_+, \bar{r}_-)]\left(\frac{1}{z\lambda}(\delta x_+, \delta x_-)\right) \times \mathfrak{F}[\mu(\delta r_1, \delta r_2)]\left(\frac{1}{z\lambda}(\bar{x}_+, \bar{x}_-)\right). \tag{A4}$$

The above result recovers the far-field speckle correlations obtained in Ref. [18].

2. Near field

We define the near-field region to be such that the propagation distance $z < \sigma_0\sigma_-/\lambda$. Since the far-field assumption implied that $\mathfrak{F}[\mu]$ is much broader than $R_0[]$ as a function of $(\bar{r}_+, \bar{r}_-)$ in Eq. (A3), the reverse is true here: $\mathfrak{F}[\mu]$ is much narrower along both dimensions here and samples R_0 effectively like a delta function in Eq. (A3). It can be explicitly seen with the following transformation.

Let $p = \frac{1}{z\lambda}(\bar{x}_+ - \bar{r}_+)$, $p' = \frac{1}{z\lambda}(\bar{x}_- - \bar{r}_-)$. Equation (A3) becomes

$$\begin{aligned}\Gamma_z &= C\int R_0(\bar{x}_+ - z\lambda p, \bar{x}_- - z\lambda p')\mathfrak{F}[\mu(\delta r_1, \delta r_2)](p, p') \\ &\quad \times e^{i\frac{k_0}{z}(\delta x_+\bar{x}_+ + \delta x_-\bar{x}_-) - i2\pi\delta x_+ p - i2\pi\delta x_- p'} dp dp' \\ &\approx R_0(\bar{x}_+, \bar{x}_-)\mu(\delta x_+, \delta x_-),\end{aligned} \tag{A5}$$

yielding the biphoton speckle correlation in the near field.

APPENDIX B: SIMULATIONS

In the simulations, we model the biphoton wavefunction propagation as Eq. (A1). While this conceptually differs from a classical field equation, in the code it is exactly like propagating a coherent field twice the dimension of the classical field. The transverse size of the simulation is 2 cm × 2 cm, with each pixel covering an area of 5 μm × 5 μm. The wavelength of the biphoton is 810 nm, as used in the experiment. The phase $\phi(x)$ of the 1D scatterer is generated by using random numbers in the range (0, 1) from a uniform distribution that are then stretched to cover the full phase range $[0, 2\pi]$. Afterward, we smoothen the profile with the "imgaussian" function in MATLAB and set the scatterer correlation length to $\sigma = 44\,\mu$m by fitting the autocorrelation of $e^{i\phi(x)}$ with a Gaussian. As shown in Fig. 1, the widths of the input state are $\sigma_- = 1$ mm and $\sigma_+ = 5$ mm (far-field of the SPDC beam is incident on the scatterer; σ_+ becomes the difference coordinate width, and σ_- becomes the sum coordinate width). In our simulations, we use the angular spectrum method to propagate each photon [40], which is more accurate than the paraxial approximation used in Eq. (A1).

The blur filter size for all the results in Fig. 2 was fixed at 200 μm. Before measuring the speckle size (determined by an autocorrelation), we removed the slowly varying envelope of the coincidence intensity by dividing the speckle image by its Gaussian blur. We then subtracted the mean, normalized with its maximum value, and put a binary threshold at 0.7. Finally, for better visualization, we rotated the resulting image by 45°.

APPENDIX C: EXPERIMENTS

The experimental setup is shown in Fig. 3(a). Here, we continue its description, starting with the vertical slit used to control the overall spatial extent of the biphoton beam. The slit is imaged onto the plane of a Holoeye spatial light modulator (HED 6010 L NIR II) using two lenses: $L2$ of focal length 7.5 cm and $L3$ of focal length 30 cm. The imaging relay lenses $L4$, $L5$ are both of focal lengths 20 cm. To mimic an ideal thin scatterer, we applied a 1D random phase to the SLM, generated by the same algorithm used in the simulations. For the experiment, we performed a Gaussian blurring in MATLAB with filter size = 8 and stretched the intensity values to the range (0, 255) to match the grayscale bit depth of the SLM.

For coincidence imaging with the EMCCD, we used the scheme outlined in Refs. [24–27]. More specifically, we calculated the coincidences as

$$\Gamma_c(x_1, x_2) \propto \sum_{k=1}^{N} I^k(x_1)I^k(x_2) - \sum_{k=1}^{N} I^k(x_1)I^{k+1}(x_2), \tag{C1}$$

where N is the number of frames and $I^k(x_1)$ represents the intensity obtained at pixel position x_1 in the kth frame. To expedite the data acquisition, we limited data collection to 1D by performing horizontal binning in the camera itself. To remove noise, we blurred the measurements with a Gaussian filter and eliminated any negative values. We also removed any nonzero self-correlations by setting to zero the values on the right diagonal (and the neighboring 15 pixels on its left and right sides).

Since the peak intensity decreases as the speckles propagate, we increased the exposure parameters for longer propagation distances. For $z = 0$ and $z = 1.5$ cm, we took 1.2 million frames with an exposure time of 0.01 s. For $z = 10$ cm, the exposure time was 0.04 s with 2 million frames. For $z = 25.5$ cm, we took 2.2 million frames with an exposure time of 0.04 s. The filter size of the Gaussian blur for $z = 0$, 1.5, 10 cm was 2.5 pixels, while that for $z = 25.5$ cm was 5 pixels.

APPENDIX D: SINGLE-PHOTON INTENSITY OF THE BIPHOTON STATE

The single-photon intensity associated with the SPDC biphoton is obtained by performing a partial trace over the partner photon. The resulting single-photon state is, in general, partially coherent. For the biphoton state considered in our work, the transverse coherence length of this reduced state is set by the biphoton correlation length. We can therefore calculate the single-photon intensity as

$$I_z(x) = \iint G^{(1)}_{\text{in}}(r, r')e^{i\phi(r)}e^{-i\phi(r')}h_z(r, x)h^*_z(r', x)\,dr\,dr', \tag{D1}$$

where the coherence at the input plane is obtained by partial tracing the biphoton wavefunction [22]: $G^{(1)}_{\text{in}}(r, r') = \int \psi_{\text{in}}(r, r_2)\psi^*_{\text{in}}(r', r_2)\,dr_2$.

Using the free-space propagation transfer function ($h_z(r, x) \propto e^{-ik_0r^2 + ik_0xr/z}$), Eq. (D1) can be further simplified. We define the speckle field $S_z(x) = \int e^{i\phi(r)}e^{-ik_0r^2 + ik_0xr/z}\,dr$ as the field produced when the scattering layer is illuminated

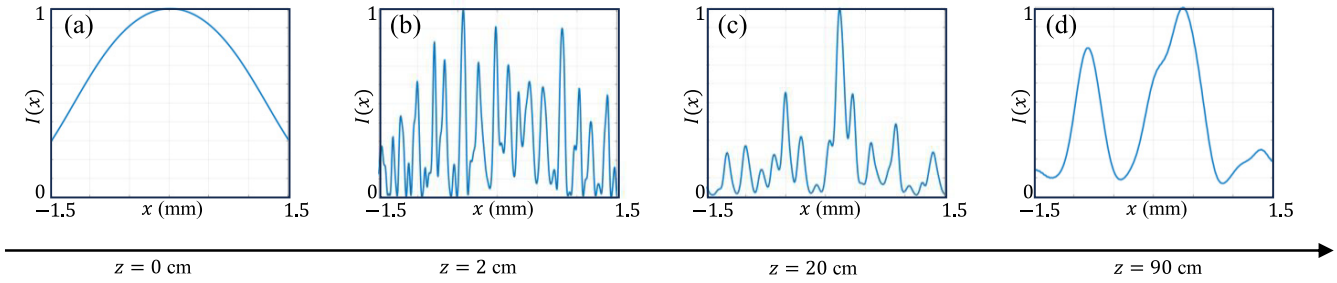


FIG. 4. Simulations of single-photon intensities (normalized) with varying z. They are obtained from the marginals of biphotons presented in Figs. 1(b)–1(e).

by a plane wave (note that the integral is taken over the illuminated area). For the source, we define its angular spectrum $A(x/z) = \iint G^{(1)}_{\text{in}}(r, r')e^{ik_0 x(r-r')/z}\,dr\,dr'$. Using these definitions, the single-photon intensity can be written as

$$I_z(x) = A(x/z) \otimes |S_z(x)|^2, \tag{D2}$$

where $\otimes$ denotes a convolution operation.

Thus, the single-photon intensity produced by a partially coherent source can be viewed as the convolution of the speckle intensity generated by plane-wave illumination with a spatial filter determined by the angular spectrum of the source. For a fully coherent source, the angular spectrum reduces to a delta function, and the above equation recovers the usual plane-wave speckle intensity at all z. For a partially coherent source, the finite width of the angular spectrum averages over different illumination angles and consequently smooths the speckle pattern. The corresponding spatial averaging scale increases with propagation distance z.

This behavior is also evident in our simulations. The single-photon marginals of the biphoton distributions shown in Fig. 4 exhibit a gradual loss of speckle contrast with increasing propagation distance, consistent with the convolution picture described.

[1] J. Leendertz, Interferometric displacement measurement on scattering surfaces utilizing speckle effect, J. Phys. E **3**, 214 (1970).

[2] I. M. Vellekoop and A. P. Mosk, Focusing coherent light through opaque strongly scattering media, Opt. Lett. **32**, 2309 (2007).

[3] J. Bertolotti, E. G. van Putten, C. Blum, A. Lagendijk, W. L. Vos, and A. P. Mosk, Non-invasive imaging through opaque scattering layers, Nature (London) **491**, 232 (2012).

[4] O. Katz, P. Heidmann, M. Fink, and S. Gigan, Non-invasive single-shot imaging through scattering layers and around corners via speckle correlations, Nat. Photonics **8**, 784 (2014).

[5] N. Antipa, G. Kuo, R. Heckel, B. Mildenhall, E. Bostan, R. Ng, and L. Waller, DiffuserCam: Lensless single-exposure 3D imaging, Optica **5**, 1 (2018).

[6] S. Aarav and J. W. Fleischer, Using speckle correlations for single-shot 3D imaging, Appl. Opt. **62**, D181 (2023).

[7] S. Aarav and J. W. Fleischer, Depth-resolved speckle correlation imaging using the axial memory effect, Opt. Express **32**, 23750 (2024).

[8] M. Rafayelyan, J. Dong, Y. Tan, F. Krzakala, and S. Gigan, Large-scale optical reservoir computing for spatiotemporal chaotic systems prediction, Phys. Rev. X **10**, 041037 (2020).

[9] I. Freund, M. Rosenbluh, and S. Feng, Memory effects in propagation of optical waves through disordered media, Phys. Rev. Lett. **61**, 2328 (1988).

[10] C. Sun, L. Waller, D. V. Dylov, and J. W. Fleischer, Spectral dynamics of spatially incoherent modulation instability, Phys. Rev. Lett. **108**, 263902 (2012).

[11] N. Bender, H. Yılmaz, Y. Bromberg, and H. Cao, Customizing speckle intensity statistics, Optica **5**, 595 (2018).

[12] N. K. Metzger, R. Spesyvtsev, G. D. Bruce, B. Miller, G. T. Maker, G. Malcolm, M. Mazilu, and K. Dholakia, Harnessing speckle for a sub-femtometre resolved broadband wavemeter and laser stabilization, Nat. Commun. **8**, 15610 (2017).

[13] J. W. Goodman, *Speckle Phenomena in Optics: Theory and Applications* (Roberts and Company Publishers, Englewood, CO, 2007).

[14] M. Giglio, M. Carpineti, and A. Vailati, Space intensity correlations in the near field of the scattered light: A direct measurement of the density correlation function $g(r)$, Phys. Rev. Lett. **85**, 1416 (2000).

[15] A. Gatti, D. Magatti, and F. Ferri, Three-dimensional coherence of light speckles: Theory, Phys. Rev. A **78**, 063806 (2008).

[16] D. Magatti, A. Gatti, and F. Ferri, Three-dimensional coherence of light speckles: Experiment, Phys. Rev. A **79**, 053831 (2009).

[17] R. Cerbino, Correlations of light in the deep Fresnel region: An extended Van Cittert and Zernike theorem, Phys. Rev. A **75**, 053815 (2007).

[18] W. H. Peeters, J. J. D. Moerman, and M. P. van Exter, Observation of two-photon speckle patterns, Phys. Rev. Lett. **104**, 173601 (2010).

[19] G. Soro, E. Lantz, A. Mosset, and F. Devaux, Quantum spatial correlations imaging through thick scattering media: Experiments and comparison with simulations of the biphoton wave function, J. Opt. **23**, 025201 (2021).

[20] S. Karan, S. Aarav, H. Bharadhwaj, L. Taneja, A. De, G. Kulkarni, N. Meher, and A. K. Jha, Phase matching in β-barium

borate crystals for spontaneous parametric down-conversion, J. Opt. **22**, 083501 (2020).
[21] M. Fedorov, Y. M. Mikhailova, and P. Volkov, Gaussian modelling and Schmidt modes of SPDC biphoton states, J. Phys. B: At. Mol. Opt. Phys. **42**, 175503 (2009).
[22] J. Schneeloch and J. C. Howell, Introduction to the transverse spatial correlations in spontaneous parametric down-conversion through the biphoton birth zone, J. Opt. **18**, 053501 (2016).
[23] M. Reichert, X. Sun, and J. W. Fleischer, Quality of spatial entanglement propagation, Phys. Rev. A **95**, 063836 (2017).
[24] H. Defienne, M. Reichert, and J. W. Fleischer, General model of photon-pair detection with an image sensor, Phys. Rev. Lett. **120**, 203604 (2018).
[25] M. Reichert, H. Defienne, and J. W. Fleischer, Massively parallel coincidence counting of high-dimensional entangled states, Sci. Rep. **8**, 7925 (2018).
[26] H. Defienne, P. Cameron, B. Ndagano, A. Lyons, M. Reichert, J. Zhao, A. R. Harvey, E. Charbon, J. W. Fleischer, and D. Faccio, Pixel super-resolution with spatially entangled photons, Nat. Commun. **13**, 3566 (2022).
[27] A. Bhattacharjee, M. K. Joshi, S. Karan, J. Leach, and A. K. Jha, Propagation-induced revival of entanglement in the angle-OAM bases, Sci. Adv. **8**, eabn7876 (2022).
[28] G. Brida, M. Genovese, and I. Ruo Berchera, Experimental realization of sub-shot-noise quantum imaging, Nat. Photonics **4**, 227 (2010).
[29] H. Di Lorenzo Pires, J. Woudenberg, and M. P. van Exter, Statistical properties of two-photon speckles, Phys. Rev. A **85**, 033807 (2012).
[30] C. W. J. Beenakker, J. W. F. Venderbos, and M. P. van Exter, Two-photon speckle as a probe of multi-dimensional entanglement, Phys. Rev. Lett. **102**, 193601 (2009).
[31] H. Defienne, M. Reichert, and J. W. Fleischer, Adaptive quantum optics with spatially entangled photon pairs, Phys. Rev. Lett. **121**, 233601 (2018).
[32] O. Lib, G. Hasson, and Y. Bromberg, Real-time shaping of entangled photons by classical control and feedback, Sci. Adv. **6**, eabb6298 (2020).
[33] J. P. Dowling, Quantum optical metrology—The lowdown on high-N00N states, Contemp. Phys. **49**, 125 (2008).
[34] V. Giovannetti, S. Lloyd, L. Maccone, and J. H. Shapiro, Sub-Rayleigh-diffraction-bound quantum imaging, Phys. Rev. A **79**, 013827 (2009).
[35] H. Defienne, W. P. Bowen, M. Chekhova, G. B. Lemos, D. Oron, S. Ramelow, N. Treps, and D. Faccio, Advances in quantum imaging, Nat. Photonics **18**, 1024 (2024).
[36] S. Aaronson and A. Arkhipov, The computational complexity of linear optics, in *Proceedings of the Forty-Third Annual ACM Symposium on Theory of Computing* (ACM, New York, 2011), pp. 333–342.
[37] B. Mollow, Photon correlations in the parametric frequency splitting of light, Phys. Rev. A **8**, 2684 (1973).
[38] S. Massar, F. Devaux, and E. Lantz, Multiphoton correlations between quantum images, Phys. Rev. A **108**, 013705 (2023).
[39] M. Hiekkamäki, R. F. Barros, M. Ornigotti, and R. Fickler, Observation of the quantum Gouy phase, Nat. Photonics **16**, 828 (2022).
[40] J. W. Goodman, *Introduction to Fourier Optics* (Roberts and Company Publishers, Englewood, CO, 2005).